Quantitative Depth Profiling Using Saturation-Equalized Photoacoustic Spectra

ROGER W. JONES* and **JOHN F. MCCLELLAND**

Ames Laboratory, U.S. Department of Energy, Iowa State University, Ames, Iowa 50011 (R.W.J., J.F.M.); and MTEC Photoacoustics, Inc., Ames, Iowa 50014 (J.F.M.)

Depth profiling using photoacoustic spectra taken at multiple scanning speeds or modulation frequencies is normally impaired by the increase in spectral saturation that occurs with decreasing speed or frequency. Photothermal depth profiling in general is also impeded by the ill conditioned nature of the mathematical problem of determining a depth profile from photothermal data. This paper describes a method for reducing the saturation level in low-speed or low-frequency spectra to the level at high speed or frequency so that all spectra have the same saturation. The conversion method requires only magnitude spectra, so it is applicable to both conventional and phase-modulation photoacoustic spectra. This paper also demonstrates a method for quantitative depth profiling with these converted spectra that makes use of prior knowledge about the type of profile existing in a sample to reduce the instabilities associated with the mathematically ill conditioned task.

Index Headings: **Depth profiling; Photoacoustic spectroscopy; PAS; Spectrum saturation.**

NOTICE

INTRODUCTION

A nondestructive depth-profiling probe for determining molecular composition is a highly desirable analysis tool, but there are few methods that provide one. Confocal spectroscopic microscopy can depth profile visible structures, but its depth resolution is approximately equal to its depth of field.[1] The resolution of Raman microscopy is also limited to its depth of field.[2] Variable-angle attenuated total reflectance gives very good resolution, but its probe depth is limited to a few micrometers at most.[3,4] Photothermal techniques have the virtue of a frequency dependent, and therefore adjustable, probe depth. Various photothermal techniques have been used for depth profiling, including the mirage effect,[5–7] the photopyroelectric effect,[8,9] and detecting the acoustic wave produced with a pulsed laser via the photoacoustic effect.[10–12] By far the most popular photothermal technique for depth profiling, however, is Fourier transform infrared (FT-IR) photoacoustic spectroscopy (PAS), in which the thermal wave is (indirectly) detected.

In PAS, intensity-modulated radiation is incident on a sample in a sealed chamber.[13,14] Heat deposited by sample absorption travels to the sample surface as a damped thermal wave. At the sample surface, the thermal wave heats the surrounding gas, modulating its pressure at the same frequency as the incident radiation. The pressure modulation is detected as sound by a microphone. Even before the widespread use of FT-IR spectrometers, PAS was used for depth profiling by chopping the incident radiation and using phase-sensitive detection. The phase of the signal depends on the average sample depth at which the incident radiation is absorbed, so for two-layer samples it is possible to select a phase roughly orthogonal to the signal from one layer, effectively isolating the spectrum of the other layer.[15,16] With the advent of the FT-IR spectrometer, PAS depth profiling became more common. The FT-IR spectrometer allows easy adjustment of the modulation frequency over a wide range, giving the user control over the PAS probe depth. Conventionally, the PAS probe depth is taken to be the thermal diffusion length, L, which is given by[13,14]

$$L = \left(\frac{D}{\pi f}\right)^{1/2} \tag{1}$$

where D is the thermal diffusivity of the sample and f is the modulation frequency of the incident radiation. For conventional FT-IR scanning, $f = v\bar{v}$, where v is the optical-path-difference (OPD) scanning speed (which is twice the mirror velocity) and $\bar{v}$ is the wavenumber. Numerous studies have been done in which the scanning speed is varied to examine a sample with a series of probe depths.[14,17–21] It has also been recognized that a method to remove saturation from PAS spectra, or "linearize" them, emphasizes peaks from components concentrated

at the surface of a sample, so this has been used to gain depth information.[22–24] Unfortunately, conventional FT-IR PAS does not provide ready access to the phase of the photoacoustic signal. The introduction of the phase-modulation FT-IR spectrometer,[25] commonly called step-scan FT-IR, provided an easier method for determining phase. In addition, the same modulation frequency applies to the full spectrum in phase modulation, so the wavenumber dependence of the thermal diffusion length is removed.[25] The capabilities of phase modulation led to several methods of visualizing signal phase and using it to interpret the depth structure of samples.[24,26] Phase modulation has resulted in increased research on using PAS for depth profiling.[23,24,26–33] Nevertheless, conventional depth profiling by frequency variation remains the more popular approach, both because of the higher cost of phase-modulation spectrometers and because of the more complicated data processing and interpretation of phase data.

For samples composed of discrete layers, layer thicknesses can be quantitatively determined from phase differences if there is no overlap[27,28] or very modest overlap[23,29] between peaks from different layers, and the theory for discretely layered samples is well understood.[34] Except for this one use, almost all FT-IR PAS depth-profiling results have been only qualitative in nature, identifying and ordering layers or detecting the presence of compositional gradients. Two impediments to FT-IR PAS depth profiling account for this limitation—optical saturation and ill conditioning.

As in other forms of spectroscopy, the PAS signal is said to be saturated when it loses its dependence on the sample absorption coefficient, α, but saturation in PAS takes a somewhat different form from that in transmission spectroscopy. For homogeneous, thermally thick ($L <$ sample thickness) samples, the photoacoustic signal is proportional to αL^2, as long as $L < 1/\alpha$, even if the sample is opaque.[13] Only when $L > 1/\alpha$ does the signal saturate; it becomes proportional to L but independent of α. In depth profiling, this means that when the modulation frequency is lowered to increase the thermal diffusion length, the amount of saturation in a spectrum increases as L approaches $1/\alpha$. Because α varies from one peak to the next, different peaks saturate at different points as the modulation frequency drops, which complicates even the qualitative interpretation of a set of spectra with differing modulation frequencies.[14,18,19,30]

The general problem of determining the depth profile that gives rise to an observed set of photoacoustic magnitudes or phases (or both) based on those observations is, in mathematical terms, ill conditioned.[35,36] That means the solution (the depth profile) is extremely sensitive to small errors in the initial data. Researchers have therefore approached this problem either by using regularization techniques to stabilize the solution recovery,[35,36] or by using intrinsically more stable approximate solutions.[37]

In this paper, we propose a solution to the saturation impediment that equalizes the degree of saturation in spectra with different thermal diffusion lengths, and we demonstrate a method that can circumvent the impediment of ill conditioning in favorable cases by making use of *a priori* knowledge about the sample structure to limit the possible depth-profile solutions. This paper describes a method for reducing the level of saturation in a low-scanning-speed or low-modulation-frequency spectrum to that in a high-speed or high-frequency spectrum. This makes the intuitive approach of comparing spectra with different probe depths to qualitatively determine depth profiles much easier. The method makes use solely of magnitude spectra, so it is applicable to both phase-modulation and conventional FT-IR PAS spectra. It relies on having one peak in a spectrum whose scanning-speed (or frequency) dependence is like that of a peak arising from a homogeneous component. The change in magnitude of this peak between the low-speed spectrum and the high-speed spectrum is used as a guide for determining how much correction for saturation is needed in the low-speed spectrum to make it the saturation-level equivalent of the high-speed spectrum. Freed of saturation distortion, these high-speed-equivalent spectra are more readily useable in determining depth profiles. They still suffer from being formally ill conditioned for quantitative depth profiling, as all photothermal data are, but we demonstrate in this paper an approach that uses them to produce good depth profiles under favorable conditions from both discretely layered samples and samples with components having continuously varying concentrations. The approach makes use of *a priori* knowledge of what type of depth profile a sample should have. With the type of profile defined, the photoacoustic data are then used to determine only the values of the parameters in the predetermined profile function. This approach constrains the possible depth-profile solutions and reduces the likelihood of erroneous results.

THEORY

The goal is to reduce the photoacoustic saturation observed in a low scanning-speed (i.e., low modulation frequency) spectrum to the same level as a high scanning-speed spectrum so that the two spectra can be compared free of saturation differences. Equation 21 of Rosencwaig and Gersho[13] is the formula for $\mathbf{Q}$, the complex envelope of the sinusoidal pressure variation that constitutes the photoacoustic signal:

$$\mathbf{Q} = \frac{\alpha I_0 \gamma P_0}{2^{3/2} k_s l_g a_g T_0 (\alpha^2 - \sigma_s^2)} \left(\frac{(\mathbf{r} - 1)(b + 1)e^{\sigma_s l} - (\mathbf{r} + 1)(b - 1)e^{-\sigma_s l} + 2(b - \mathbf{r})e^{-\alpha l}}{(g + 1)(b + 1)e^{\sigma_s l} - (g - 1)(b - 1)e^{-\sigma_s l}} \right) \tag{2}$$

where α is the optical absorption coefficient, I_0 is the incident light flux, γ is the heat capacity ratio of the gas, P_0 and T_0 are the ambient pressure and temperature in the photoacoustic cell, l is the sample thickness, l_g is the gas thickness, and for material i (where i can be g, s, or b, for gas, sample, or backing) k_i is the thermal conduc-

tivity, C_i is the heat capacity, ρ_i is the density, $D_i = k_i/\rho_i C_i$ is the thermal diffusivity, $a_i = 1/L_i = (\pi f/D_i)^{1/2}$ is the thermal diffusion coefficient, L_i is the thermal diffusion length, f is the modulation frequency, and $\sigma_i = (1 + j)a_i$. In addition, $b = k_b a_b/(k_s a_s)$, $g = k_g a_g/(k_s a_s)$, and $\mathbf{r} = \frac{1}{2}(1 - j)\alpha/a_s$.

For thermally and optically thick samples, $\sigma_s l \gg 1$ and $\alpha l \gg 1$, so the $e^{-\sigma_s l}$ and $e^{-\alpha l}$ terms can be dropped, which simplifies Eq. 2 to the following:

$$\mathbf{Q} = \frac{\alpha I_0 \gamma P_0}{2^{3/2} k_s l_g a_g T_0 (\alpha^2 - \sigma_s^2)} \left(\frac{\mathbf{r} - 1}{g + 1} \right) \tag{3}$$

From the definitions given above, it can be shown that $\sigma_s = \alpha/\mathbf{r}$. Substituting this for σ_s gives the following:

$$\mathbf{Q} = \frac{I_0 \gamma P_0 \mathbf{r}^2}{2^{3/2} k_s l_g a_g T_0 \alpha (\mathbf{r} + 1)(g + 1)} \tag{4}$$

Let the ratio of the high-speed spectrum to the low-speed spectrum at any given wavenumber be $\mathbf{R}$. This equals the ratio of $\mathbf{Q}$ at the high-speed frequency and $\mathbf{Q}$ at the low-speed frequency. The only quantities on the right side of Eq. 4 that depend on frequency are $\mathbf{r}$ and a_g, so all of the other variables cancel out when calculating $\mathbf{R}$:

$$\mathbf{R} = \frac{\mathbf{Q}_h}{\mathbf{Q}_l} = \frac{\mathbf{r}_h^2 a_{gl}(\mathbf{r}_l + 1)}{\mathbf{r}_l^2 a_{gh}(\mathbf{r}_h + 1)} \tag{5}$$

where the l and h subscripts refer to the two frequencies. If the frequencies of the data point at the low and high speeds are f and Nf, respectively, then $\mathbf{r}_h = \mathbf{r}_l/N^{1/2}$ and $a_{gh} = a_{gl}N^{1/2}$. Equation 5 therefore simplifies to

$$\mathbf{R} = \frac{\mathbf{r}_l + 1}{N(\mathbf{r}_l + N^{1/2})} \tag{6}$$

Unfortunately, $\mathbf{r}$ depends on both the absorption coefficient at each wavenumber and the thermal properties of the sample, so Eq. 6 by itself cannot be used to determine $\mathbf{R}$ from just the observed spectra. A substitute for $\mathbf{r}$ must be derived from the spectra. This can be done by scaling a spectrum according to how saturated it is; that is, by putting it on a scale of 0 to 1 where 1 is the completely saturated, maximum possible photoacoustic signal, which is the signal for an infinite absorption coefficient. The maximum possible signal, $\mathbf{Q}_{max}$, can be derived from Eq. 4:

$$\mathbf{Q}_{max} = \lim_{\alpha \to \infty} \mathbf{Q} = \frac{I_0 \gamma P_0 \mathbf{r}}{2^{3/2} k_s l_g a_g T_0 \alpha (g + 1)} \tag{7}$$

The data points of the spectrum scaled from 0 to 1, $\mathbf{Q}_{sc}$, can then be calculated by ratioing $\mathbf{Q}$ and $\mathbf{Q}_{max}$:

$$\mathbf{Q}_{sc} = \frac{\mathbf{Q}}{\mathbf{Q}_{max}} = \frac{\mathbf{r}}{\mathbf{r} + 1} \tag{8}$$

Combining Eqs. 6 and 8 allows $\mathbf{r}_l$ to be eliminated, and $\mathbf{R}$ can be written in terms of $\mathbf{Q}_{sc}$, or $\mathbf{Q}_{sc}$ can be written in terms of $\mathbf{R}$:

$$\mathbf{R} = \frac{1}{N^{3/2} + \mathbf{Q}_{sc}(N - N^{3/2})} \tag{9}$$

$$\mathbf{Q}_{sc} = \frac{N^{3/2}\mathbf{R} - 1}{N\mathbf{R}(N^{1/2} - 1)} \tag{10}$$

where $\mathbf{Q}_{sc}$ is the scaled version of the low-speed spectrum. Equations 9 and 10 are valid for unnormalized photoacoustic spectra without any instrumental effects (e.g., the frequency-dependent throughput of a spectrometer). In practical terms, normalized spectra must be used so as to eliminate instrumental effects. Using normalized spectra changes $\mathbf{R}$ because of the frequency dependence of the photoacoustic signal from the normalization reference. Assuming the reference-material signal has a magnitude with f^{-1} dependence and a frequency-independent phase, as is expected for a good reference,[13,38] then $\mathbf{R}_n = N\mathbf{R}$, where $\mathbf{R}_n$ is $\mathbf{R}$ for use with normalized spectra. Equations 9 and 10 can then be rewritten for normalized spectra:

$$\mathbf{R}_n = \frac{1}{N^{1/2} + \mathbf{Q}_{sc}(1 - N^{1/2})} \tag{11}$$

$$\mathbf{Q}_{sc} = \frac{N^{1/2}\mathbf{R}_n - 1}{\mathbf{R}_n(N^{1/2} - 1)} \tag{12}$$

In the above equations, $\mathbf{R}_n$ and $\mathbf{Q}_{sc}$ are vectors, having both magnitude and phase. Only the magnitudes of these vectors, R_n and Q_{sc}, can be derived from ordinary magnitude spectra, so Eqs. 11 and 12 must be recast for the magnitudes:

$$R_n = \frac{1}{[N + 2N^{1/2}(1 - N^{1/2})q_r + (1 - N^{1/2})^2 Q_{sc}^2]^{1/2}} \tag{13}$$

$$Q_{sc} = \frac{[NR_n^2 - 2N^{1/2}\rho_r + 1]^{1/2}}{R_n(N^{1/2} - 1)} \tag{14}$$

where q_r and ρ_r are the real components of the vectors $\mathbf{Q}_{sc}$ and $\mathbf{R}_n$, respectively. The real components can be related to the magnitudes:

$$q_r = \frac{\alpha L + 1}{\alpha L} Q_{sc}^2 \tag{15}$$

$$\rho_r = \left(1 + \frac{(N^{1/2} - 1)(\alpha L + 2)}{\alpha^2 L^2 + 2\alpha L + 2} \right) R_n^2 \tag{16}$$

The αL product can be written in terms of either Q_{sc} or R_n, as needed:

$$\alpha L = \frac{Q_{sc}^2 + Q_{sc}(2 - Q_{sc}^2)^{1/2}}{1 - Q_{sc}^2} \tag{17}$$

$$\alpha L = \frac{1 - N^{1/2}R_n^2 - [-NR_n^4 + 2NR_n^2 - 2N^{1/2}R_n^2 + 2R_n^2 - 1]^{1/2}}{R_n^2 - 1} \tag{18}$$

Substituting Eqs. 15 and 17 into Eq. 13 allows R_n to be determined from Q_{sc}, while substituting Eqs. 16 and 18 into Eq. 14 gives Q_{sc} from R_n. Figure 1 shows how R_n and Q_{sc} are related for various values of N. Note that the value for αL calculated from Eq. 17 or 18 is the product of the absorption coefficient and thermal diffusion length only if a peak arises from a homogeneous component. Although the above discussion refers to two different scanning speeds, it applies equally well when data are collected at two different modulation frequencies unrelated to scanning speed, such as in phase-modulation spectroscopy. The composite-piston model of McDonald and Wetsel[38] can also be used as the starting point for
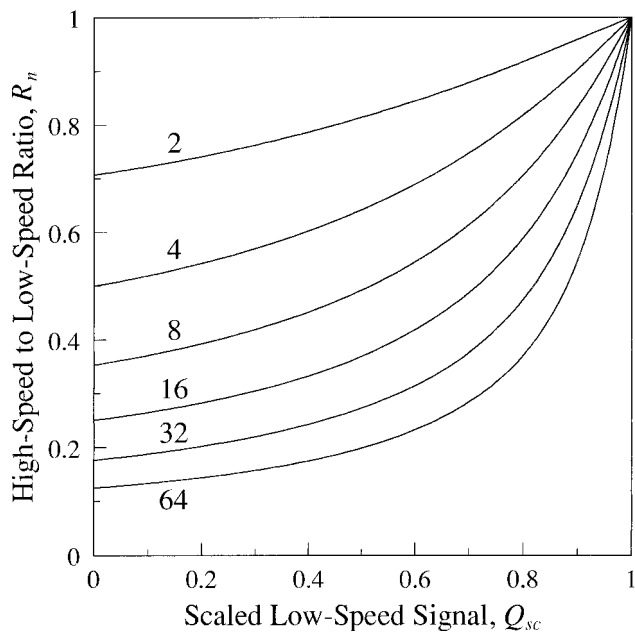
FIG. 1. Relation between the ratio, R_n, of photoacoustic magnitudes at two different scanning speeds and the magnitude of the photoacoustic signal at the lower speed, Q_{sc}, on a scale where a completely saturated signal equals one. The ratio of the scanning speeds is marked for each curve.

developing the speed-conversion equations if the physical oscillation from thermal expansion by the sample is neglected. Equations 13 through 18 can be derived from Eq. 41 of McDonald and Wetsel if the thermal expansion coefficient (their β_T) is set to zero.

EXPERIMENTAL

Two Bio-Rad FTS 60A FT-IR spectrometers fitted with MTEC Model 200 photoacoustic detectors were used for all spectrum acquisition. One spectrometer was controlled by a Bio-Rad SPC 3200 Workstation running Unix-based DDS. It acquired the data in Figs. 2 through 5. The other used a Digital Celebris 90 MHz Pentium PC running Windows NT 4 based Win-IR Pro. It acquired the data in Figs. 6 through 8. All data were taken using normal (non-phase modulation) scanning at 8 cm^{-1} resolution. The number of scans coadded depended on scanning speed. The Bio-Rad spectrometers denote scanning speed in terms of HeNe laser-fringe modulation frequency. There were 10 scans at 50 Hz (0.00316 cm/s OPD velocity), 20 at 100 Hz (0.00633 cm/s), 41 at 200 Hz (0.0127 cm/s), 82 at 400 Hz (0.0253 cm/s), 164 at 800 Hz (0.0506 cm/s), 512 at 2.5 kHz (0.158 cm/s), 1024 at 5 kHz (0.316 cm/s), 2048 at 10 kHz (0.633 cm/s), 4096 at 20 kHz (1.27 cm/s), and at 40 kHz (2.53 cm/s) either 8192 scans for the data in Figs. 2 through 5 or 32 768 scans for the data in Figs. 6 through 8. Glassy carbon (MTEC Photoacoustics) was used as the normalization reference. The photoacoustic detectors were helium purged and desiccant (magnesium perchlorate) was placed in the detectors beneath the samples. The spectra were translated using GRAMS/386 into spreadsheet-file format, then the speed conversion and most other data processing were performed using Lotus 1-2-3. The non-linear least-squares curve fitting was done using SigmaPlot. A thermal diffusivity of 0.0010 cm^2/s for polyethylene terephthalate (PET) was used for all calculations, based on data from Anderson and Acton.[39]

Three sample types were used in the experiments. A 1.3-mm-thick poly(methyl methacrylate) disk was used for the homogeneous-sample work. A layered sample was constructed using a previously described method[29] from a 6-μm sheet of PET (Chemplex) and 1.6-mm-thick polycarbonate (GE Lexan®). A brass ring (6-mm i.d.) was placed on top of the layered sample during data collection so that any delaminations at the edge of the sample were hidden. A set of artificially weathered PET samples were used for depth profiling a sample gradient. These were 0.3-mm-thick extruded sheets containing varying amounts of Tinuvin 360®. The weathering was 1088 hours exposure according to Method A of ASTM G26,[40] which consists of xenon arc light filtered by borosilicate (daylight) filters. The conditions were continuous illumination at 0.35 W/m^2 (at 340 nm) and 63 °C black-panel temperature with an 18 min water spray repeated every 2 h. The brass ring was also placed on top of these samples during spectrum collection.

To confirm the depth profiling results from the speed-conversion method, the weathered PET samples were destructively analyzed using a method of successive lapping.[41] In this method, the thickness of the sample is measured and a photoacoustic spectrum of the sample is acquired at a high scanning speed and thus at a small thermal diffusion length. A few micrometers of the sample are then removed using the MTEC MicroLap, another high-scanning-speed spectrum is acquired, and the sample thickness (or more accurately, the combined thickness of the sample and its MicroLap mount) is again measured. This lapping, scanning, and thickness measuring cycle is repeated until all of the thickness of interest within the sample has been analyzed. The variation of peak heights with lapping depth then provides a direct measure of variations in component concentrations through the lapped portion of the sample. In the present study, the spectra were acquired at a 20 kHz scanning speed, corresponding to a 2.8 μm thermal diffusion length (at the 3271 cm^{-1} position of the peak used in the analysis, and based on a thermal diffusivity of 0.0010 cm^2/s). A fresh 12-μm-grit lapping disk was installed on the MicroLap at the beginning of each sample analysis, and 204 g of weight was used to supply the force pressing the sample against the lapping disk. The lapping time between successive spectra varied from 2 s to 3 min, depending on the amount of material to be removed and how worn the lapping disk had become during the analysis. We have used the thermal diffusion length of the photoacoustic measurement as the probe depth of the measurement, which means that the sample depth for the measured peak heights prior to any lapping is 3 μm. (We have rounded to the nearest micrometer because the sample-thickness measurements are accurate only to ±1 μm at best.) The sample depths for successive spectra are then the total thickness of material lapped off plus 3 μm. This depth scale gives a better fit with the speed-conversion results than assuming a 0 μm depth for the pre-lapping measurement. One of the samples (that containing 2% additive) required a modification of this scale. The first lapping performed on this sample changed the measured
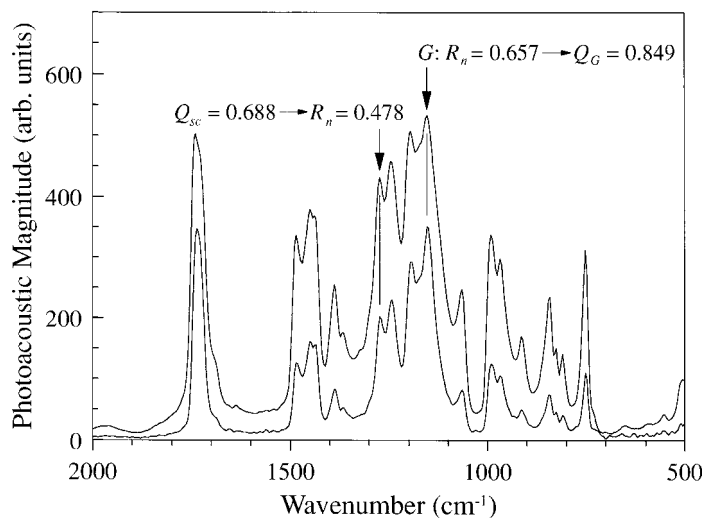
FIG. 2. Spectra of a thick sample of PMMA taken at scanning speeds of 2.5 and 40 kHz, and the conversion-parameter values for the guide peak, G, and an example peak.
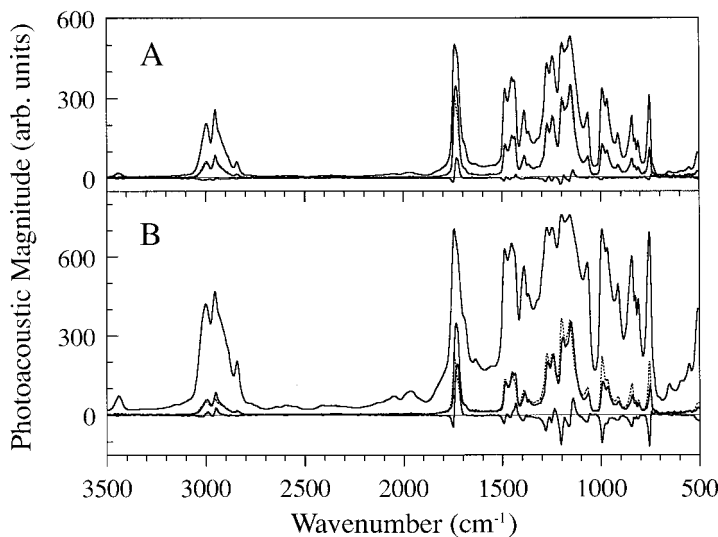

FIG. 3. Conversion of two low-speed spectra of PMMA to high-speed equivalents. (**A**) The 2.5 and 40 kHz spectra from Fig. 2, the 2.5 kHz spectrum after conversion to 40 kHz equivalence (dotted line), and the difference spectrum between the true 40 kHz spectrum and the 40 kHz-equivalent spectrum. (**B**) As in **A**, except using starting spectra at 200 Hz and 40 kHz.

thickness by an unusually large amount (15 μm) but had little effect on spectrum-peak height. The next three lappings after that each removed a decreasing thickness and had an increasing effect on peak height. Apparently, this sample had a few high points on its surface, which were all that was being taken off at first. The "depth" of the sample surface, therefore, had to be assigned for this one sample. Given the decaying-exponential gradient expected for this sample (see Results and Discussion), the greatest change in peak height with depth should occur at the sample surface measurement (i.e., at a probe depth of 3 μm). Accordingly, we have assigned the measurement after the second lapping (when the total measured reduction in thickness was 19 μm) a depth of 1 μm, which places the greatest peak-height change with depth between 2 and 3 μm.

RESULTS AND DISCUSSION

Performing a speed conversion can best be illustrated using spectra of a homogeneous sample. Figure 2 shows two spectra of a thermally thick disk of poly(methyl methacrylate) (PMMA). The taller of the two spectra was taken at a scanning speed of 2.5 kHz and the smaller at 40 kHz, so the frequency ratio, N, is 16. The process begins by scaling the low-speed spectrum. The behavior of a peak, G, in the two spectra will be used to guide the scaling. The peak must arise from a homogeneous component of the sample so that the height of the peak varies with scanning speed according to the Rosencwaig and Gersho theory.[13] In Fig. 2, the peak at 1153 cm^{-1} has been selected to be G. If the heights of peak G are h_h and h_l in the high- and low-speed spectra, respectively, then $R_n = h_h/h_l$, and Q_{sc} for the peak, which we will call Q_G, can be calculated from Eq. 14. The peak-height ratio of G in Fig. 2 is 0.657, so from Eq. 14 (or reading from Fig. 1), Q_G is 0.849. Now that Q_G is known, the scaling for the rest of the spectrum is straightforward because the scaling is linear with a scaling factor of Q_G/h_l. If a data point in the low-speed spectrum has a value Y, so that it is y times the value of peak G, then it will have a value

of yQ_G in the scaled spectrum; $Q_{sc} = yQ_G = YQ_G/h_l$ for that point. For example, the second peak marked in Fig. 2 is at 1273 cm^{-1}. In the low-speed spectrum, the magnitude of this peak is 81% the magnitude of G, so Q_{sc} at 1273 cm^{-1} is 81% of Q_G, or 0.688. Once the whole spectrum has been scaled and all of the Q_{sc} values are known, Eq. 13 is used to determine R_n for each data point. For the 1273 cm^{-1} peak of the example, R_n calculated from Eq. 13 (or read from Fig. 1) is 0.478. Each data point in the starting, low-speed spectrum (not the scaled spectrum) is multiplied by the R_n calculated for it to produce the high-speed-spectrum equivalent.

For a homogeneous sample, the high-speed equivalent should be identical to the spectrum acquired at high speed. Figure 3A shows the example pair of PMMA spectra from Fig. 2 along with the results of the example speed conversion. The high-speed equivalent is plotted as a dotted line, but it is hard to discern because it overlaps the true high-speed spectrum. The fourth spectrum in Fig. 3A, centered around zero magnitude, is an error spectrum, the difference between the true high-speed spectrum and the high-speed equivalent (true minus equivalent). The error spectrum shows that there are two kinds of errors present in the speed-conversion result. First, the 1736 cm^{-1} peak is slightly under predicted by the speed conversion. Second, the errors all have a derivative-like form, tending to be positive-valued on the low-wavenumber side of a peak and negative-valued on the other side. This arises from a phenomenon not predicted by the Rosencwaig–Gersho theory. As the amount of saturation grows, the observed location of a spectrum peak slowly shifts to higher wavenumber. For the example in Fig. 3A, this shift is less than the spacing between adjacent data points, even for the strongest, most saturated features. Nevertheless, it results in the speed conversion predictions being slightly too small on the low-wavenumber side and slightly too large on the other side of the strongest peaks.

Figure 3B shows a second example using the same PMMA sample, but with a much larger frequency ratio between the starting spectra. The tall spectrum was acquired at 200 Hz, and the smaller, solid-line spectrum is the 40 kHz spectrum used before, so N is now 200. The dotted spectrum is the high-speed equivalent calculated from the 200 Hz spectrum, again using 1153 cm^{-1} as the guide peak. An error spectrum is also plotted as before. Overall, the speed-converted spectrum is qualitatively similar to the true high-speed spectrum, but the closeness of the match varies substantially from peak to peak. Between 1000 and 2000 cm^{-1}, the error spectrum in Fig. 3B looks largely like an amplified version of the Fig. 3A error spectrum. This comes from the saturation-related peak shift being larger here than in the previous example, so the derivative-like errors are greater. Outside the 1000 to 2000 cm^{-1} range, the error spectrum shows another trend. The error-spectrum features are negative-going at low wavenumbers and positive-going at high wavenumbers. This is a general pattern we have observed for a variety of samples once N becomes large enough; partly saturated peaks in the low-speed spectrum tend to be too large after speed conversion at wavenumbers below the guide-peak location and too small above the guide peak, with the error generally increasing with distance from the guide peak. We have observed this trend with phase-modulation spectra as well, so it is not related to the variation in modulation frequency with wavenumber across rapid-scan spectra. Using a different material as the background reference may help in individual cases by providing different normalization scaling. Here, however, we have used glassy carbon throughout because we found it to be the best general background reference.

The thermal diffusion length, which is proportional to $f^{-1/2}$, is conventionally taken as the approximate probe depth of a photoacoustic measurement. A set of speed-converted spectra at various scanning speeds (and so various frequencies) therefore provides a qualitative view of the depth dependence in a sample. This view is much clearer than that from unconverted spectra because the obscuring effects of unequal saturation levels have been removed. The utility of speed-converted spectra can be extended even further. With some foreknowledge of what kind of depth profile should be present in a sample, quantitative depth profiles can be derived from the speed-converted data.

Two decay effects control the depth sensitivity of speed-converted spectra; the attenuation of illuminating radiation as it is absorbed in the sample, and the decay of the thermal wave as it travels from the point of radiation absorption to the sample surface. Formally, speed conversion removes the effects of illumination attenuation, but if the average value of the depth-varying absorption coefficient is sufficiently large, virtually all of the illuminating radiation will be absorbed within one thermal diffusion length of the sample surface. No information can be gathered from depths where the illumination does not reach. Accordingly, the rest of this paper will be limited to the case where speed conversion reduces the effects of radiation attenuation to the point that attenuation may be ignored over the range of depths being probed. Within this limitation, the depth sensitivity of speed-converted spectra is controlled solely by the ex-

ponentially decaying thermal wave. The thermal diffusion coefficient, a, which equals $1/L$, is the rate constant for this decay. The photoacoustic signal is therefore proportional to the product of the absorption coefficient and the fraction of the decayed thermal wave that reaches the sample surface, integrated over the full thickness of the sample:

$$S \propto L^{-1} \int_0^\infty \alpha(x) e^{-x/L} \, dx \tag{19}$$

where S is the normalized, speed-converted photoacoustic signal; the L^{-1} outside the integral is a normalization factor; and it is assumed the sample is thermally thick (i.e., the sample thickness is much greater than L), so that the integration can extend to infinity. Also implicit in Eq. 19 is the assumption that the speed conversion does not improperly correct a peak height. The equations for speed conversion are based on a homogeneous-sample model. If depth-related composition changes cause a peak to grow so much over the range of scanning speeds used that the peak appears to be entering saturation, then the speed conversion will inappropriately "correct" it, and it will appear too large in the speed-converted spectrum. The 560 cm^{-1} peak in Fig. 4 is an example of this and is discussed below.

As previously discussed, determining $\alpha(x)$ from a set of S values measured at various thermal diffusion lengths, is an "ill conditioned" problem.[35,36] Although the general solution for determining depth profiles from spectra may be ill conditioned, if there is *a priori* knowledge of what kind of depth profile a sample should have, so that only a few parameters need to be determined, then the speed-converted spectra can often be used with Eq. 19 to determine the specific profile. The simplest non-trivial case is a sample composed of a discrete layer of thickness l on top of a thermally thick substrate. At a given wavenumber, the absorption coefficient has a constant value, α_1, for $0 < x < l$, and a second constant value, α_2, for $x > l$. For such an $\alpha(x)$, Eq. 19 becomes the following:

$$S = C(\alpha_1 + (\alpha_2 - \alpha_1)e^{-l/L}) \tag{20}$$

where C is a proportionality constant. This assumes there is negligible difference between the thermal properties of the substrate and overlayer. The normalized, speed-converted photoacoustic signal can be considered an exponential function of $1/L$, with a rate constant of l. The thickness of the discrete layer can be determined by fitting Eq. 20 to a set of measured S values.

Figure 4 shows spectra for a sample consisting of a 6-μm layer of PET on top of a 1.7-mm-thick polycarbonate substrate. The bottom panel in Fig. 4 shows normalized photoacoustic spectra of the sample taken at scanning speeds of 40 kHz (thick solid line), 10 kHz (dot-dash line), 2.5 kHz (thin solid line), and 400 Hz (dotted line). The reader is reminded that these frequencies are modulation rates for the HeNe laser beam within the spectrometer and not for the infrared beam incident on the sample. The top panel in Fig. 4 shows the same 40 kHz spectrum and the other spectra converted to 40 kHz equivalents. The guide-point position for the conversions was 1111 cm^{-1}, which is on the flat shoulder of the broad 1130 cm^{-1} band. Using this flat area reduces the possi-
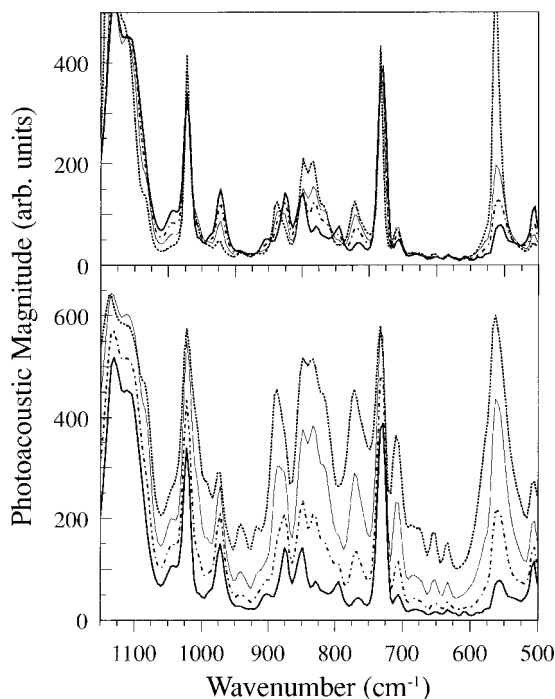
FIG. 4. Spectra of a sample consisting of a 6-μm layer of PET on a thick polycarbonate substrate taken at 40 kHz (thick solid line), 10 kHz (dot-dash line), 2.5 kHz (thin solid line), and 400 Hz (dotted line) scanning speeds. Lower panel; spectra as acquired. Upper panel; the same spectra as in the lower panel after conversion to 40 kHz equivalence.
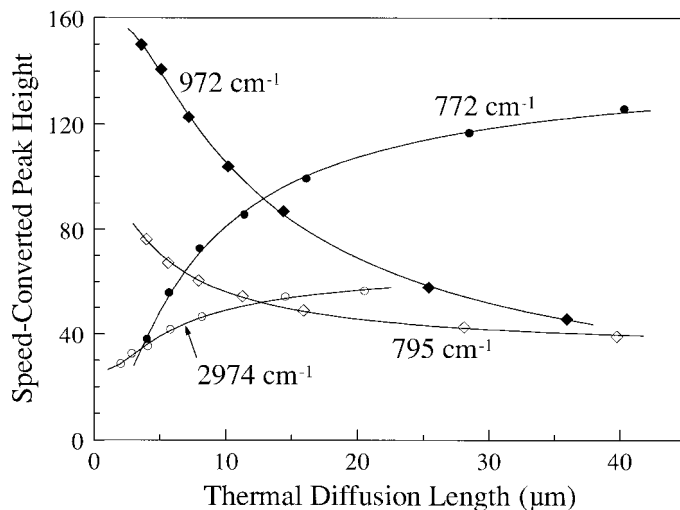

FIG. 5. Peak heights as a function of thermal diffusion length for five peaks taken from seven speed-converted spectra (including those in the upper panel of Fig. 4) of a sample consisting of a 6-μm layer of PET on a polycarbonate substrate.

bility of the previously described peak-shifting affecting the accuracy of the guide-point values. Prior to speed conversion, the 40 kHz spectrum is the smallest throughout, indicating that, as usual, the signal magnitude increases with decreasing scanning speed everywhere except the most saturated features. After speed conversion, this behavior is gone, and each peak has its own trend, qualitatively indicating the depth-related sample structure. Those peaks that grow with decreasing scanning speed grow with increasing thermal diffusion length, so they must arise from the polycarbonate substrate. Those peaks that shrink with decreasing scanning speed and increasing thermal diffusion length must come from the PET layer. The strongest bands in the 40 kHz spectrum (730, 1020, and 1130 cm^{-1}) change little with scanning speed after conversion, indicating that they are strong PET bands in which almost all of the incident beam intensity is absorbed within the PET. The polycarbonate band at 560 cm^{-1} is an example of a peak that is improperly corrected by the speed conversion because the peak grows so large at low scanning speeds. In the speed-converted spectra, the 560 cm^{-1} peak height grows steadily between the 40 and 2.5 kHz spectra but then leaps to a much higher value at 400 Hz. In the spectra prior to conversion, the 560 cm^{-1} peak is smaller than the strong, highly saturated PET bands, except in the 400 Hz spectrum. At 400 Hz, the 560 cm^{-1} peak is as tall as these bands, so the conversion treats it as a highly saturated band; its Q_{sc} and R_n values are near 1, and the peak height remains near its original value of 600 after conversion. The speed-conversion equations properly correct the growth of large peaks arising from homogenous com-

ponents, but it can distort large peaks whose growth is principally caused by sample structure.

Performing a least-squares fit of the function on the right side of Eq. 20 to a set of speed-converted heights for a selected peak determines l, the thickness of the top layer, but which peak do you select? There are three factors to keep in mind when choosing peaks to analyze. First, because of the potential distortion of large nonhomogeneous peaks, like the 560 cm^{-1} example, it is best to use features that remain moderate in size after speed conversion. Second, because of the ill conditioning of this problem, it is best to analyze several peaks and use only those that give the best fit (e.g., the smallest rms errors) to the model function. Third, because the observed peak location shifts with scanning speed, as discussed above, the wavenumber location of a peak at low scanning speeds may be higher than it is at high scanning speeds, so there is some uncertainty in exactly which data point to use for a given peak. If the wavenumber location of the peak as observed in high-speed spectra is chosen, then of course at high speed the chosen location is on the band peak, but at low speeds it is not. For the low-speed location, the reverse is true. This means that using the high-speed location yields apparent peak heights that are larger at high speeds and smaller at low speeds than using the low-speed location would yield. As a result, the high-speed peak position generally gives a smaller value for l than the low-speed position does because the S vs. L curve flattens out faster with increasing L for the high-speed location. Again, choosing the position that gives the best fit to the model function is generally best, as long as that fit is physically meaningful. For speed-converted peaks that grow with increasing thermal diffusion length (i.e., arise from the substrate), the high-speed peak position may fit the model function well and yet give a negative value for $C\alpha_1$ in Eq. 20, which implies a negative value for α_1, which is impossible. When this occurs, the l value determined at that wavenumber position is too small, and a higher wavenumber position should be used for the peak.
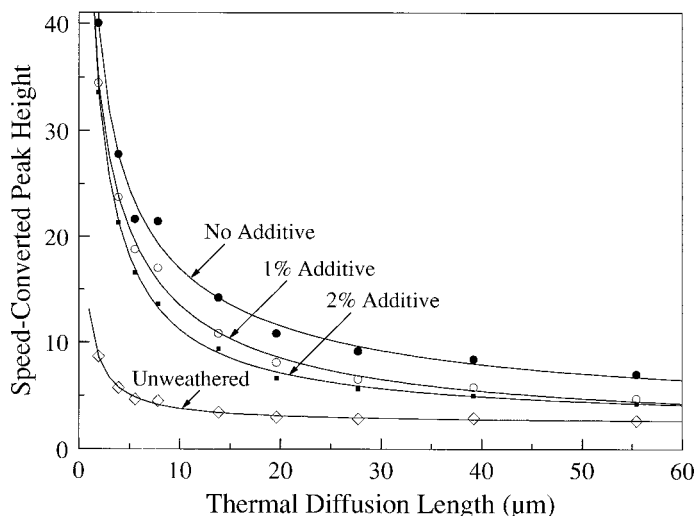
FIG. 6. Heights of the 3271 cm^{-1} hydroxyl peak in speed-converted spectra of one unweathered and three weathered PET samples. Data for the three weathered samples are identified by their concentration of ultraviolet stabilizer. The discrete markers are the observed peak heights, and the curves are least-squares fits of Eq. 22 (with $n = 2$) to the observed points.

Figure 5 shows the peak-height behavior of four peaks from the PET-on-polycarbonate sample spectra. The data points shown are those for the spectra in Fig. 4, along with points from spectra taken at scanning speeds of 20 kHz, 5 kHz, and 800 Hz. The smooth curves are least-squares fits of the Eq. 20 function to the observed data points. These four peaks give the best fits among a dozen different wavenumber positions tested. The l values determined from these fits are 6.5 μm at 772 cm^{-1}, 4.7 μm at 795 cm^{-1}, 10.5 μm at 972 cm^{-1}, and 5.8 μm at 2974 cm^{-1}. Although the 10.5 μm value from 972 cm^{-1} is obviously high in comparison to the known thickness of 6 μm, there would be no objective reason to exclude this result if the true thickness were not known; the root-mean-square error of the 972 cm^{-1} fit is smaller than that for 772 cm^{-1}. Combining these four measurements gives a layer thickness of 6.9 ± 2.5 μm, in agreement with the known value. The rms error of this is large because of the ill-conditioned nature of the problem. Layer thicknesses in discretely layered samples can be determined more straightforwardly and often more accurately using phase measurements on peaks having little overlap with bands from another sample layer.[23,27–29] When there is moderate overlap between peaks from different layers, however, phase measurements cannot be used to determine layer thicknesses, but the present method can be used.

Determining depth profiles rather than just layer thicknesses is where using Eq. 19 and speed-converted spectra can be superior to phase measurements. One common profile type is an exponential gradient consisting of one or a sum of exponentials:

$$\alpha(x) = c_0 + \sum_{i=1}^{n} c_i e^{d_i x} \qquad (21)$$

where x is sample depth, and c_0, c_i, and d_i are all constants. From Eq. 19, the photoacoustic signal from a sample with such a gradient is

$$S = C\left(c_0 + \sum_{i=1}^{n} \frac{c_i}{1 - d_i L}\right) \qquad (22)$$

where C is a proportionality constant. We examined artificially weathered PET sheets as examples of materials with two-exponential ($n = 2$) gradients. The set consisted of three samples weathered for 1088 hours and an unweathered control. The weathered samples contained 0, 1, and 2 wt % of the ultraviolet stabilizer Tinuvin® 360. We recorded spectra at nine scanning speeds from 40 kHz to 50 Hz and speed converted them, again using 1111 cm^{-1} as the guide peak. The hydroxyl peak at 3271 cm^{-1} in the resulting spectra showed the gradient most clearly. The discrete data points in Fig. 6 are the speed-converted hydroxyl peak heights for all four samples. Least-squares fits to these peak heights using Eq. 22 with two exponentials produce the parameter values in Table I and the smooth curves in Fig. 6. The results are qualitatively reasonable; the hydroxyl peak increases in size and the gradient extends to greater thermal diffusion lengths for decreasing amounts of the stabilizer. The unweathered sample has a small, nearly constant hydroxyl peak at most thermal diffusion lengths, but shows an increase at small thermal diffusion lengths, which may indicate some hydroxyl species on the sample surface. The smooth curves in Fig. 7 are the double-exponential depth profiles calculated from the parameters in Table I. Again, the results are reasonable. In terms of the Table I parameters, all three weathered samples have small d_1 values and substantially larger d_2 values. This means that the first exponentials taper off slowly with depth and account for most of the shape of the curves in Fig. 7. The second exponentials drop to negligible values at shallow depths, so they affect only the near-surface results. The d_1 values decrease with decreasing additive concentration, indicating that the hydroxyl gradient extends to a greater depth with decreasing additive. The large d_1 and extremely small d_2 for the unweathered sample mean its gradient is essentially a very shallow single exponential.

To determine whether these profiles were correct, we

TABLE I. Hydroxyl gradient parameters from least-squares fits of speed-converted peak heights.

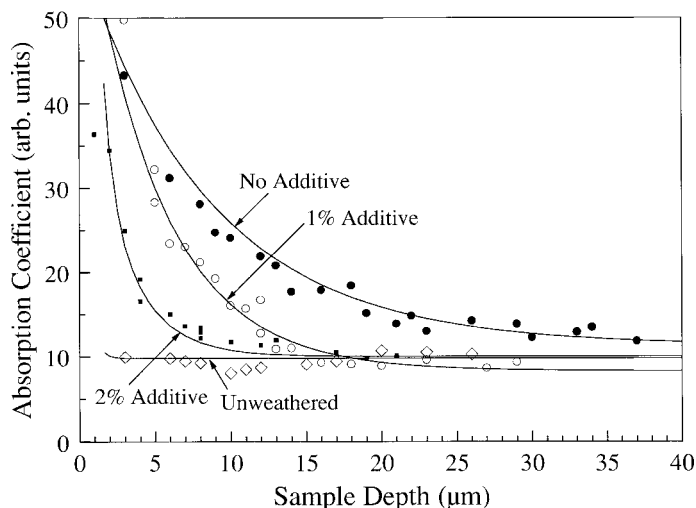| Equation 22 parameters	Double-exponential fits				Single-exponential fit
	Unweathered	2% additive	1% additive	No additive	No additive
Cc_0	12.9	2.51	1.69	3.09	4.73
Cc_1	42.3	18.1	28.1	22.0	67.0
d_1	−2.95	−0.395	−0.203	−0.117	−0.468
Cc_2	−10.5	89.1	266.	1300.	
d_2	-1.0×10^{-12}	−1.67	−10.2	−34.6	

FIG. 7. Quantitative depth profiles of the 3271 cm^{-1} peak in the same weathered and unweathered PET samples as in Fig. 6. The smooth curves are the calculated depth profiles based on the parameters in Table I and Eqs. 21 and 22. The discrete data points are observed peak heights from spectra taken as material was lapped off the surface of each sample.

destructively analyzed the samples using the successive lapping technique described in the Experimental section.[41] The successive lapping produced the discrete data points in Fig. 7. The arbitrary vertical units are not the same for the successive-lapping and speed-conversion methods, so the speed-conversion curves have been scaled and offset vertically *as a group* in Fig. 7 to give the best match with the successive-lapping data. That is, the same factor (2.14) was used to scale all four curves, and the same factor (4.65) was used to offset all four. Somewhat better fits could have been achieved if each curve were scaled and offset individually, but universal factors were used because the only purpose was to bring the two arbitrary scales into agreement.

The match between the two data sets is very good, demonstrating that non-trivial depth profiles can be obtained nondestructively by photoacoustic analysis. The limitation stated earlier must be emphasized, however; the type of gradient curve to be fitted must be known in advance in order to achieve a reliable depth profile. If a plausible but incorrect type of curve is chosen, it is possible to get a precise fit to the peak-height data that produces an inaccurate depth profile. The weathered PET data provide a case in point. Figure 8A shows the same speed-converted peak-height data for the no-additive sample, as in Fig. 6, and the same two-exponential-based fit of the data as before (solid line). Figure 8A also shows a least-squares fit based on a single exponential (dashed line), the parameters for which are given in Table I. Both are good fits; the rms error of the one-exponential fit is only 1.11 times that of the two-exponential fit, so the two-exponential fit is only slightly better. Figure 8B, however, shows that the resulting depth profiles differ substantially in how well they match the successive-lapping data. Each profile has been scaled and offset vertically to give the best least-squares fit to the lapping data, but the one-exponential profile (dashed line) is obviously inferior. (Because the two-exponential curve has been scaled and offset individually in Fig. 8B, it fits the lap-
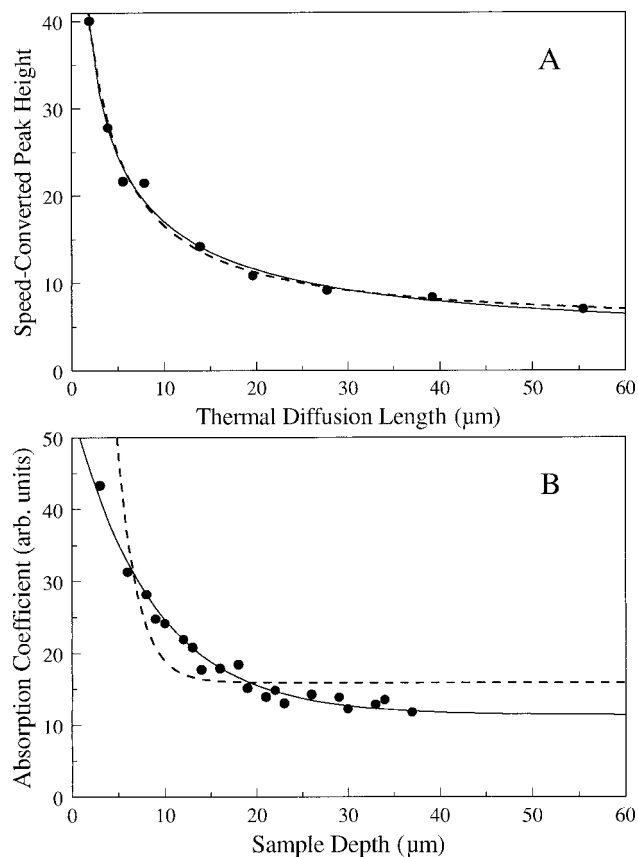

FIG. 8. (**A**) The speed-converted peak heights of the 3271 cm^{-1} peak in weathered PET containing no additive (discrete points) and the least squares fits to these points assuming a double-exponential gradient (solid line) or a single-exponential gradient (dashed line). The peak heights and double-exponential fit are the same as in Fig. 6. (**B**) The depth profiles derived from the double-exponential (solid line) and single-exponential (dashed line) fits in **A** compared to the observed peak height during the microlapping of the sample. The lapping points are the same ones as in Fig. 7.

ping data better than in Fig. 7, where universal scaling and offsetting were used.) Among the weathered PET samples, the differences between the two- and one-exponential profiles decrease as the weathering effects decrease, as signified by the decreasing values of both Cc_2 and d_2 with increasing additive concentration. Nevertheless, the two-exponential profile is always clearly better.

CONCLUSION

A method for making the level of saturation the same in photoacoustic spectra taken at different scanning speeds or modulation frequencies has been developed. These saturation-equalized spectra make the depth-related structure in samples much clearer. In addition, an approach for quantitatively depth profiling samples with these spectra has been demonstrated. The approach makes use of *a priori* knowledge about the sample structure to restrict the possible depth-profile outcomes and reduce or avoid the ill-conditioned nature of the mathematical problem.

1. T. Wilson and C. Sheppard, *Theory and Practice of Scanning Optical Microscopy* (Academic Press, London, 1984).
2. G. Turrell and J. Corset, *Raman Microscopy: Developments and Applications* (Academic Press, London, 1996).
3. R. A. Shick, J. L. Koenig, and H. Ishida, Appl. Spectrosc. **50,** 1082 (1996).
4. F. M. Mirabella, "Attenuated Total Reflection Spectroscopy," in *Modern Techniques in Applied Molecular Spectroscopy,* F. M. Mirabella, Ed. (Wiley Scientific, New York, 1998), Chap. 4, pp. 127–184.
5. B. Mongeau, G. Rousset, and L. Bertrand, Can. J. Phys. **64,** 1056 (1986).
6. W. Faubel, G. R. Hofmann, S. Janssen, and B. S. Seidel, "Quantitative Analysis of Atmospheric Copper Corrosion Productions by Photoacoustic FTIR Spectrometry and Photothermal Deflection Method," in *Photoacoustic and Photothermal Phenomena: Tenth International Conference,* F. Scudieri and M. Bertolotti, Eds. (American Institute of Physics, Woodbury, NY, 1999), CP 463, pp. 661–663.
7. S. W. Fu and J. F. Power, Appl. Spectrosc. **54,** 127 (2000).
8. J. F. Power and M. C. Prystay, Appl. Spectrosc. **49,** 725 (1995).
9. M. Chirtoc, I. Chirtoc, D. Paris, J.-S. Antoniow, and M. Egée, "Photopyroelectric (PPE) Study of Water Migration in Humidified Laminated Starch Sheets," in *Photoacoustic and Photothermal Phenomena: Tenth International Conference,* F. Scudieri and M. Bertolotti, Eds. (American Institute of Physics, Woodbury, NY, 1999), CP 463, pp. 646–648.
10. A. Beenen, G. Spanner, and R. Niessner, Appl. Spectrosc. **51,** 51 (1997).
11. C. Kopp and R. Niessner, Anal. Chem. **71,** 4663 (1999).
12. C. Kopp and R. Niessner, "Depth Resolved Photoacoustic Measurements with Pulsed Excitation," in *Photoacoustic and Photothermal Phenomena: Tenth International Conference,* F. Scudieri and M. Bertolotti, Eds. (American Institute of Physics, Woodbury, NY, 1999), CP 463, pp. 27–30.
13. A. Rosencwaig and A. Gersho, J. Appl. Phys. **47,** 64 (1976).
14. J. F. McClelland, R. W. Jones, S. Luo, and L. M. Seaverson, "A Practical Guide to FT-IR Photoacoustic Spectroscopy," in *Practical Sampling Techniques for Infrared Analysis,* P. B. Coleman, Ed. (CRC Press, Boca Raton, Florida, 1993), Chap. 5, pp. 107–144.
15. D. M. Anjo and T. A. Moore, Photochem. Photobiol. **39,** 635 (1984).
16. J. W. Nery, O. Pessoa, Jr., H. Vargas, F. de A. M. Reis, A. C. Gabrielli, L. C. M. Miranda, and C. A. Vinha, Analyst (Cambridge, U.K.) **112,** 1487 (1987).
17. C. Q. Yang, R. R. Bresee, and W. G. Fateley, Appl. Spectrosc. **41,** 889 (1987).
18. P. A. Dolby and R. McIntyre, Polymer **32,** 586 (1991).
19. L. E. Jurdana, K. P. Ghiggino, I. H. Leaver, C. G. Barraclough, and P. Cole-Clarke, Appl. Spectrosc. **48,** 44 (1994).
20. L. Gonon, O. J. Vasseur, and J.-L. Gardette, Appl. Spectrosc. **53,** 157 (1999).
21. B. D. Pennington, R. A. Ryntz, and M. W. Urban, Polymer **40,** 4795 (1999).
22. R. O. Carter III, Appl. Spectrosc. **46,** 219 (1992).
23. J. F. McClelland, S. J. Bajic, R. W. Jones, and L. M. Seaverson, "Photoacoustic Spectroscopy," in *Modern Techniques in Applied Molecular Spectroscopy,* F. M. Mirabella, Ed. (Wiley Scientific, New York, 1998), Chap. 6, pp. 221–265.
24. E. Y. Jiang, W. J. McCarthy, and D. L. Drapcho, Spectroscopy **13**(2), 21 (1998).
25. M. J. Smith, C. J. Manning, R. A. Palmer, and J. L.Chao, Appl. Spectrosc. **42,** 546 (1988).
26. E. Y. Jiang and R. A. Palmer, Anal. Chem. **69,** 1931 (1997).
27. E. Y. Jiang, R. A. Palmer, N. E. Barr, and N. Morosoff, Appl. Spectrosc. **51,** 1238 (1997).
28. D. L. Drapcho, R. Curbelo, E. Y. Jiang, R. A. Crocombe, and W. J. McCarthy, Appl. Spectrosc. **51,** 453 (1997).
29. R. W. Jones and J. F. McClelland, Appl. Spectrosc. **50,** 1258 (1996).
30. M. G. Sowa and H. H. Mantsch, Appl. Spectrosc. **48,** 316 (1994).
31. Y. Kano, S. Akiyama, T. Kasemura, and S. Kobayashi, Polym. J. **27,** 339 (1995).
32. M. W. C. Wahls and J. C. Leyte, J. Appl. Phys. **83,** 504 (1998).
33. M. W. Urban, C. L. Allison, G. L. Johnson, and F. Di Stefano, Appl. Spectrosc. **53,** 1520 (1999).
34. E. Y. Jiang, R. A. Palmer, and J. L. Chao, J. Appl. Phys. **73,** 460 (1995).
35. R. J. W. Hodgson, J. Appl. Phys. **76,** 7524 (1994).
36. J. F. Power, Analyst (Cambridge, U.K.) **121,** 451 (1996).
37. A. Harata and T. Sawada, J. Appl. Phys. **65,** 959 (1989).
38. F. A. McDonald and G. C. Wetsel, Jr., J. Appl. Phys. **49,** 2313 (1978).
39. D. R. Anderson and R. U. Acton, "Thermal Properties", in *Encyclopedia of Polymer Science and Technology,* H. F. Mark, N. G. Gaylord, and N. M. Bikales, Eds. (Wiley-Interscience, New York, 1970), vol. 13, pp. 780–1, Table 4.
40. *Annual Book of ASTM Standards,* Vol. 14.04 (American Society for Testing and Materials, West Conshohocken, Pennsylvania, 2000), Standard Practice G26-96, pp. 455–464.
41. J. F. McClelland, R. W. Jones, and S. J. Bajic, "Photoacoustic Spectroscopy", in *Handbook of Vibrational Spectroscopy,* J. M. Chalmers and P. R. Griffiths, Eds. (Wiley, London, 2002), vol. 2, pp. 1231–1251.